JOURNAL OF SYNCHROTRON RADIATION

Volume 28 (2021)

Supporting information for article:

Millisecond timescale reactions observed via X-ray spectroscopy in a 3D microfabricated fused silica mixer

Diego A. Huyke, Ashwin Ramachandran, Oscar Ramirez-Neri, Jose A. Guerrero-Cruz, Leland B. Gee, Augustin Braun, Dimosthenis Sokaras, Brenda Garcia-Estrada, Edward I. Solomon, Britt Hedman, Mario U. Delgado-Jaime, Daniel P. DePonte, Thomas Kroll and Juan G. Santiago

Supplementary information for

Millisecond timescale reactions observed via X-ray spectroscopy in a 3D microfabricated fused silica mixer

Diego A. Huyke,[1] Ashwin Ramachandran,[1] Oscar Ramirez-Neri,[2] Jose A. Guerrero-Cruz,[2] Leland B. Gee,[1] Augustin Braun,[1] Dimosthenis Sokaras,[3] Brenda Garcia-Estrada,[2] Edward I. Solomon,[1,3] Britt Hedman,[3] Mario U. Delgado-Jaime,[2] Daniel P. DePonte,[4] Thomas Kroll,[3,*] and Juan G. Santiago[1,*]

[1] *Stanford University, Stanford, California 94305, USA*
[2] *University of Guadalajara, 44430 Guadalajara, Mexico*
[3] *Stanford Synchrotron Radiation Lightsource, SLAC National Accelerator Laboratory, Stanford University, Menlo Park, CA 94025, USA*
[4] *Linac Coherent Light Source, SLAC National Accelerator Laboratory, Stanford University, Menlo Park, CA 94025, USA*

* To whom correspondence should be addressed. E-mails: tkroll@slac.stanford.edu and juan.santiago@stanford.edu

Content

S1. Details of numerical model

This section reports the values of physical properties used, the mesh generation procedure, and the mesh convergence analyses for the numerical models. These models were used to solve the fluid flow and species transport fields within the domain, and they were implemented in COMSOL Multiphysics 5.5 (COMSOL Inc., Sweden). Simulations were input physical properties as reported elsewhere (Table S1).

Fluid flow meshes were generated using COMSOL's automatic meshing feature with specified minimum and maximum element sizes of d_{mesh} and $3d_{mesh}$, respectively. d_{mesh} was varied between 1.8 and 100 μm. Swept meshes were implemented in regions of high aspect ratios (0.25 mm < x < 2.87 mm and x > 6.00 mm, where x is the streamwise position). Species transport meshes were generated with an adaptive refinement and swept mesh scheme (Fig. S1).

A mesh convergence study (Phan *et al.*, 2015) was performed to verify the simulation grid-independence (Fig. S2). The relative convergence parameter $c(g)$ was calculated for each of various simulations with an increasing number of mesh elements. $c(g)$ is given by

$$c(g) = \sqrt{\frac{\int \left(g - g_{ref}\right)^2 dxdydz}{\int \left(g_{ref}\right)^2 dxdydz}}, \tag{S1}$$

where g is a solution (e.g., velocity magnitude u, pressure p, and sample c_{sa} and sheath c_{sh} concentrations), g_{ref} is the solution from the reference mesh, and y and z are respectively the spanwise and transverse positions. Note the reference mesh is taken to be the most refined mesh with the greatest number of elements simulated (Fig. S2). Lower values of $c(g)$ correspond to solutions which approach that of the reference mesh. Convergence thresholds range from 1 to 2 × 10^{-3} (Muller *et al.*, 2012). A threshold of 5 × 10^{-3} was chosen here as a tradeoff between accuracy and computational time.

Table S1. Physical properties and nominal values for physical constants used in the simulations.

Variable	Description	Value	Units	Reference
η	Dynamic viscosity, water	1×10^{-3}	Pa s^{-1}	(COMSOL Inc., 2019)
ρ	Density, water	998	kg m^{-3}	(COMSOL Inc., 2019)
D_{sa}	Diffusivity, fluorescein	4.25×10^{-10}	m^2 s^{-1}	(Culbertson *et al.*, 2002)
D_{sh}	Diffusivity, rhodamine B	4.27×10^{-10}	m^2 s^{-1}	(Culbertson *et al.*, 2002)
D_{I-}	Diffusivity, iodide	1.24×10^{-9}	m^2 s^{-1}	(Darrall & Oldham, 1968)
$D_{\mathrm{Fe(CN)_6^{3-}}}$	Diffusivity, ferricyanide	7.20×10^{-10}	m^2 s^{-1}	(Konopka & McDuffie, 1970)
$D_{\mathrm{Fe(CN)_6^{4-}}}$	Diffusivity, ferrocyanide	6.66×10^{-10}	m^2 s^{-1}	(Konopka & McDuffie, 1970)
$D_{\mathrm{H_2Asc}}$	Diffusivity, ascorbic acid	1.05×10^{-9}	m^2 s^{-1}	(Shamim & Baki, 1980)
k_2	Second order decay rate	0.35 - 194.07	mM^{-1} s^{-1}	(Tonomura *et al.*, 1978)

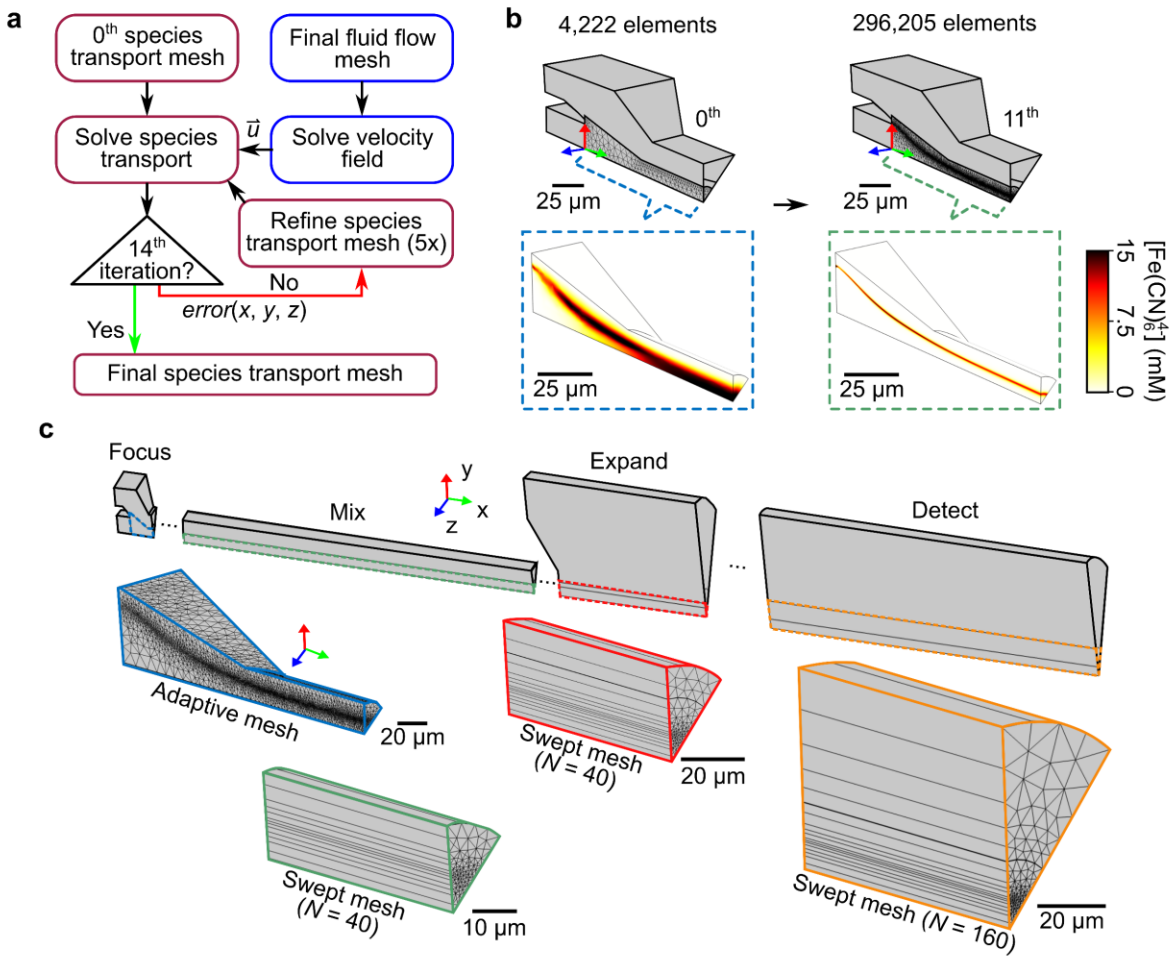

Fig. S1. Combined adaptive refinement and swept mesh generation scheme for species transport model. (a) Adaptive mesh refinement scheme (implemented for 0 mm < x < 0.25 mm) flow chart. Given a mesh and corresponding solution (e.g., species concentrations), this scheme estimates the local numerical error $error(x, y, z)$. Following, the input mesh is refined up to five times in regions of large error and the process is repeated. We term one cycle of this entire process a mesh iteration. We here increased the number of mesh elements by a factor of about 1.05 during each refinement and a maximum of 14 iterations were performed for each flow condition. (b) Example initial (left) and final (right) focusing region mesh distributions as well as the resulting ferrocyanide concentration fields $[\mathrm{Fe(CN)_6^{4-}}]$ for the same conditions as Fig. 5 of the main text. (c) Isometric views of a species transport mesh (after ten iterations) which shows the adaptive mesh and high aspect ratio, swept mesh-generated regions. Each of the three swept mesh regions featured N swept elements. The element types used were tetrahedra, prisms, triangles, quads, edge, and vertex.

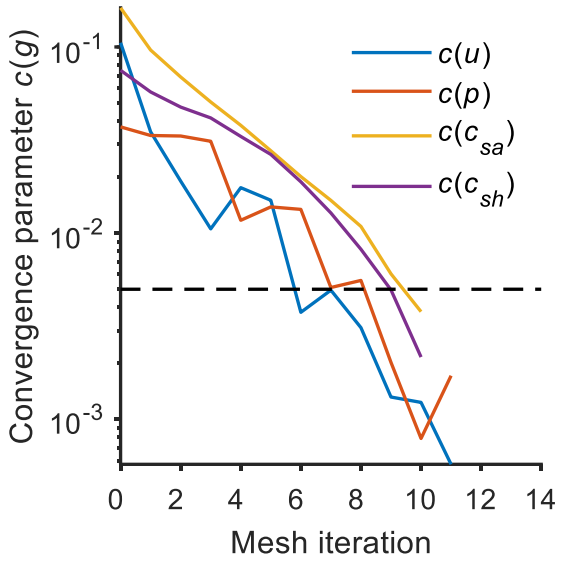

Fig. S2. Mesh convergence parameter $c(g)$ versus mesh iteration number and evaluated for the velocity magnitude u, pressure p, and the concentrations of sample c_{sa} and sheath c_{sh} fields. The dashed black line represents the threshold $c(g)$ value (= 5×10^{-3}). This threshold value was used as the criterion to select the grid-independent mesh. Note the fluid flow and species transport simulations used separate meshes as well as mesh refinement techniques. Hence, the reference mesh for the fluid flow model required 12 iterations, while the reference mesh for the species transport required 11 iterations. The fluid flow mesh was refined everywhere (all x) and the reference mesh consisted of 9.2×10^6 elements. The species transport mesh was refined only in the focusing region (0 mm $< x <$ 0.25 mm) and that reference mesh consisted of 3.0×10^5 elements. In turn, the chosen fluid flow and species transport meshes had 2.4×10^6 and 2.0×10^5 elements, respectively. The species transport mesh refinement was carried separately for each flow condition. All data is for Q_{sa} = 30 µL min^{-1}, Q_{sh} = 1 mL min^{-1}, $c_{sa,0}$ = 20 mM, and $c_{sh,0}$ = 100 mM.

S2. Scaling of the sample stream expansion length L_{exp}

We here propose and fit physical scaling theories for the sample stream deceleration (or expansion) length L_{exp} . L_{exp} is defined here as the distance between the exit of the mixing stage and the location where the sample stream achieves 95% its terminal velocity within the downstream capillary (inset of Fig. S3). The expression is

$$L_{exp} = x_e - L_{foc} - L_{mix}, \tag{S2}$$

where x_e is given by the condition that

$$u_{sa}(x_e) = 0.95 \frac{2Q_{sh}}{\pi\left(W_{cap}/2\right)^2}, \tag{S3}$$

L_{foc} is the length of the focusing stage (= 0.15 mm), L_{mix} is the length of the mixing stage (= 2.7 mm), u_{sa} is the velocity along the center ($y = z = 0$) axis, Q_{sh} is the sheath flow rate, and

W_{cap} is the internal diameter of the downstream capillary (= 0.5 mm). The velocity field in Eq. (S3) is given by the numerical solutions to the 3D Navier-Stokes equations.

First, we hypothesize L_{exp} is a function of Q_{sh}, W_{cap}, and the kinematic viscosity of water η. Dimensional analysis was used to obtain two dimensionless groups given by

$$\pi = \frac{L_{exp}}{W_{cap}}, \tag{S4}$$

and

$$Re_{sh} = \frac{4Q_{sh}}{\pi\eta W_{cap}}. \tag{S5}$$

Note π is a geometric ratio while Re_{sh} is a Reynolds number based on the bulk fluid velocity in the polyimide capillary and the polyimide capillary diameter. Simulations were used to predict the variation of L_{exp} as a function of Q_{sh} (Fig. S3). Given the observed linear trend, we hypothesized a fit of the form

$$\pi = KRe_{sh}, \tag{S6}$$

where K is a non-dimensional constant. We here obtained $K = 0.22$ using a linear least squares fitting. Hence, L_{exp} is given by

$$L_{exp} = 0.22W_{cap}Re_{sh}. \tag{S7}$$

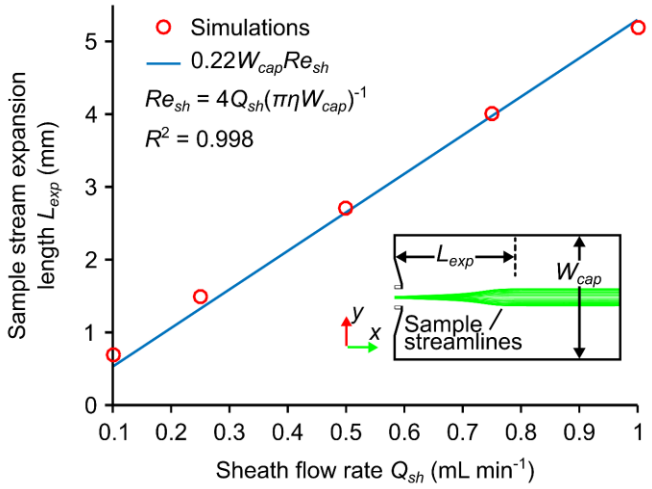

Fig. S3. Sample stream expansion (or deceleration) length L_{exp} versus sheath flow rate Q_{sh} for constant sample flow rate Q_{sa} = 30 µL min^{-1}. Shown are simulation results and a linear fit. The fit is a function of Q_{sh}, the kinematic viscosity of water η, and the width of the downstream capillary W_{cap}. The inset on the bottom right shows the downstream capillary region with green sample streamlines superposed.

S3. Residence time and residence time uncertainty for varied flow conditions

We here report the residence time t and residence time uncertainty σ_t as a function of x for various sheath flow rates between 0.5 and 1.5 mL min^{-1} (Fig. S4).

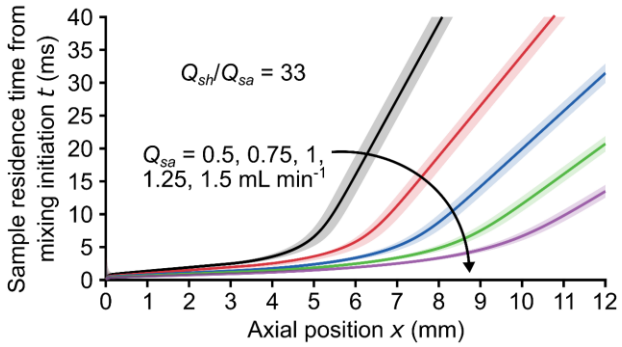

Fig. S4. Average sample residence time t (solid lines) versus mixer axial position x for varied sheath flow rates Q_{sh} between 0.5 and 1.5 mL min^{-1} and fixed sheath to sample flow rate Q_{sh}/Q_{sa} = 33. The residence time uncertainty σ_t (shaded regions) is governed by flow dispersion (associated with the nonuniform sample velocity profile) and beam smearing (associated with the finite transit time that sample molecules take to cross the X-ray beam length). All lines have similar slopes for $x < 3$ mm (the region within the fused silica chip). Downstream of that position, sample stream expansion and deceleration (a function of Q_{sh}) occur in the polyimide capillary.

S4. 3D hydrodynamic focusing with separate sample and sheath dyes

This section provides further validation of 3D hydrodynamic focusing in the fused silica chip region of the mixer. To this end, z-stack slices and isosurfaces from confocal experiments are qualitatively compared to simulations.

Isosurfaces for the sample and sheath species were constructed in MATLAB (R2019b, Mathworks, USA) from 3D concentration fields obtained from simulations and z-stack images from confocal experiments. First, a threshold value, or isovalue, for concentration (for simulations) or fluorescence intensity measurements (for confocal experimental images) was assigned. Subsequently, only voxels within a specified range of the isovalue are shown in the 3D rendering of the fields. The result was a 3D surface which shows the profile of all regions of the mixer which match a specified concentration (or fluorescence intensity measurement). This process was implemented for the sample and sheath species data.

Results show good qualitative agreement between experiments and simulations for both moderate and high sheath to sample flow rate conditions (Figs. S5 and S6, respectively). Note, however, that the limitations of the imaging technique (see Appendix C of the main text) result in nonuniform illumination and apparently "rough" isosurfaces for the experimental data.

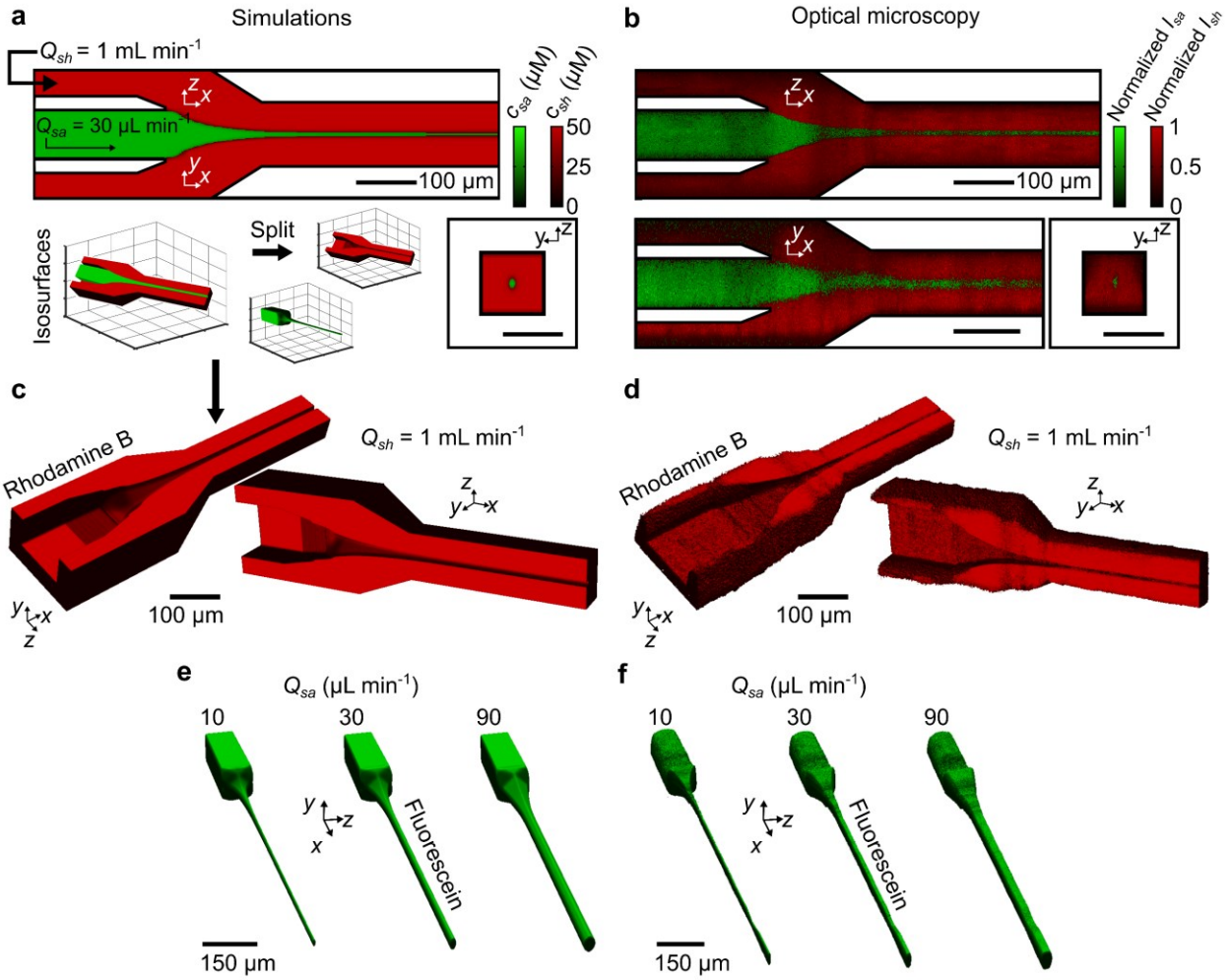

Fig. S5. 3D visualizations of sample and sheath concentrations from simulations and experiments for moderate sheath to sample flow rate Q_{sh}/Q_{sa} conditions ranging from 11 to 100. Good qualitative agreement is observed. (a) Superposed sample (fluorescein, green) and sheath (rhodamine B, red) concentration fields near the focusing and mixing regions, predicted by simulations. Shown are cross-sections at the z and y = 0 positions (identical due to the device symmetry) as well as at x = 300 µm. The bottom left of (a) depicts the separation of the red and green channels to construct fluorescein and rhodamine B isosurfaces. (b) Superposed experimental measurements of sample and sheath fluorescence intensity fields for the same locations as (a). (c) Isosurfaces of rhodamine B concentration from simulations, shown for a half-volume (in the depth direction) of the mixer. (d) Experimentally measured isosurfaces of rhodamine B fluorescence intensity. The data in (b-d) is for the same flow conditions as (a). (e) Isosurfaces of fluorescein concentration from simulations. (f) Experimental isosurfaces of fluorescein intensity. The data in (e-f) is for fixed Q_{sh} = 1 mL min^{-1} and varied Q_{sa}.

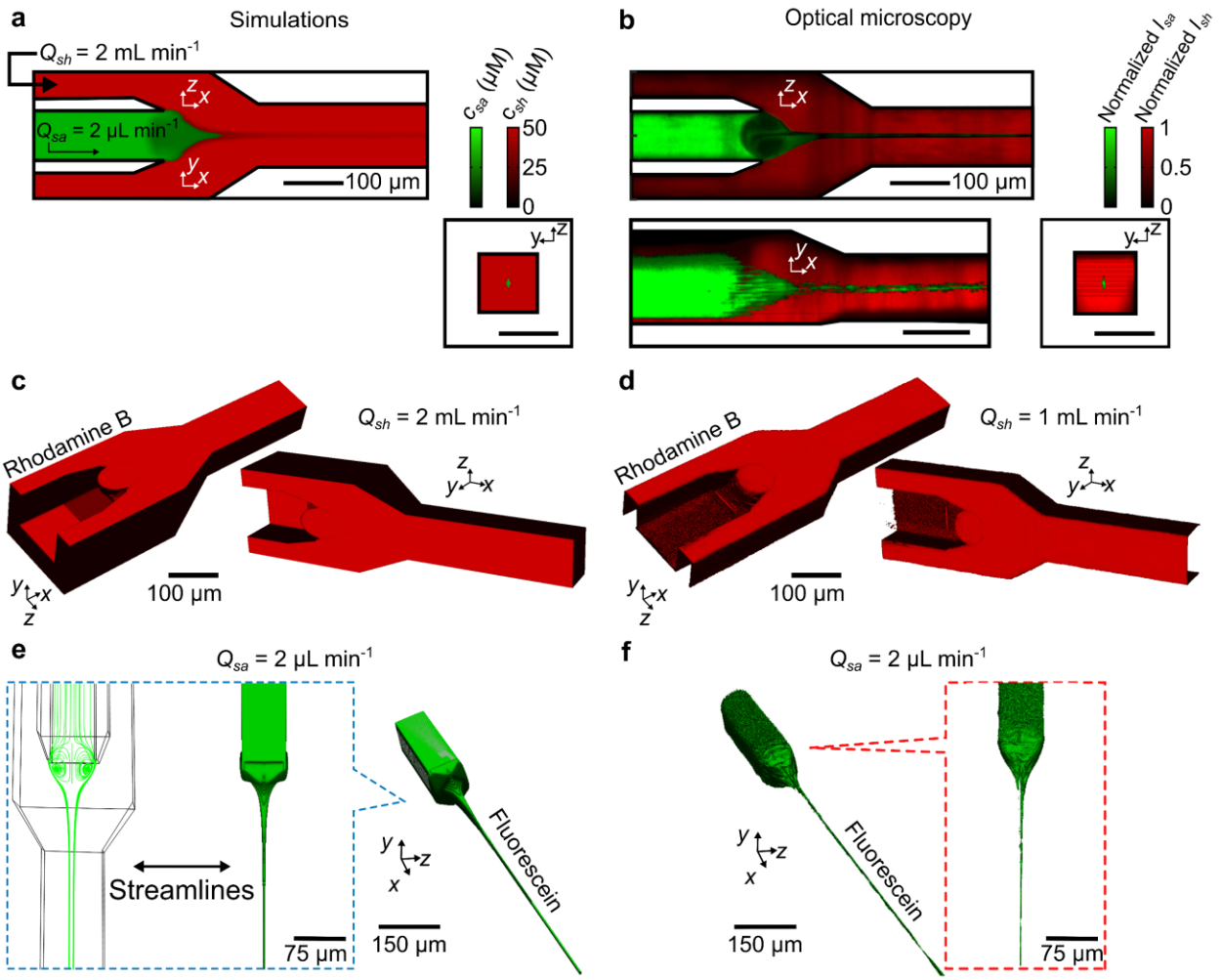

Fig. S6. 3D visualizations of sample and sheath concentrations from simulations and experiments for a high sheath to sample flow rate Q_{sh}/Q_{sa} = 1000 condition. Good qualitative agreement is observed. (a) Superposed sample and sheath concentration fields predicted by simulations. Shown are cross-sections at the z and y = 0 positions as well as at x = 300 µm. (b) Superposed experimental measurements of sample and sheath fluorescence intensity fields for the same locations as (a). (c) Isosurfaces of rhodamine B concentration from simulations, shown for a half-volume (in the depth direction) of the mixer. (d) Experimentally measured isosurfaces of rhodamine B fluorescence intensity. (e) Isosurface of fluorescein concentration from simulation. The inset (blue box) shows streamlines seeded at x = 0 as well as a top view of the fluorescein isosurface. The streamlines provide a clearer view of the recirculatory flow that appears near the sample channel exit at this flow condition. (f) Experimentally measured isosurfaces of fluorescein fluorescence intensity. The data in all panels is for the same flow conditions as (a).

S5. Fluid flow setup at X-ray beamline

We here provide a detailed schematic and image of the fluid flow setup used at the X-ray beamline as well as a representative log of the flow rate delivered to the mixer over a 2 h period.

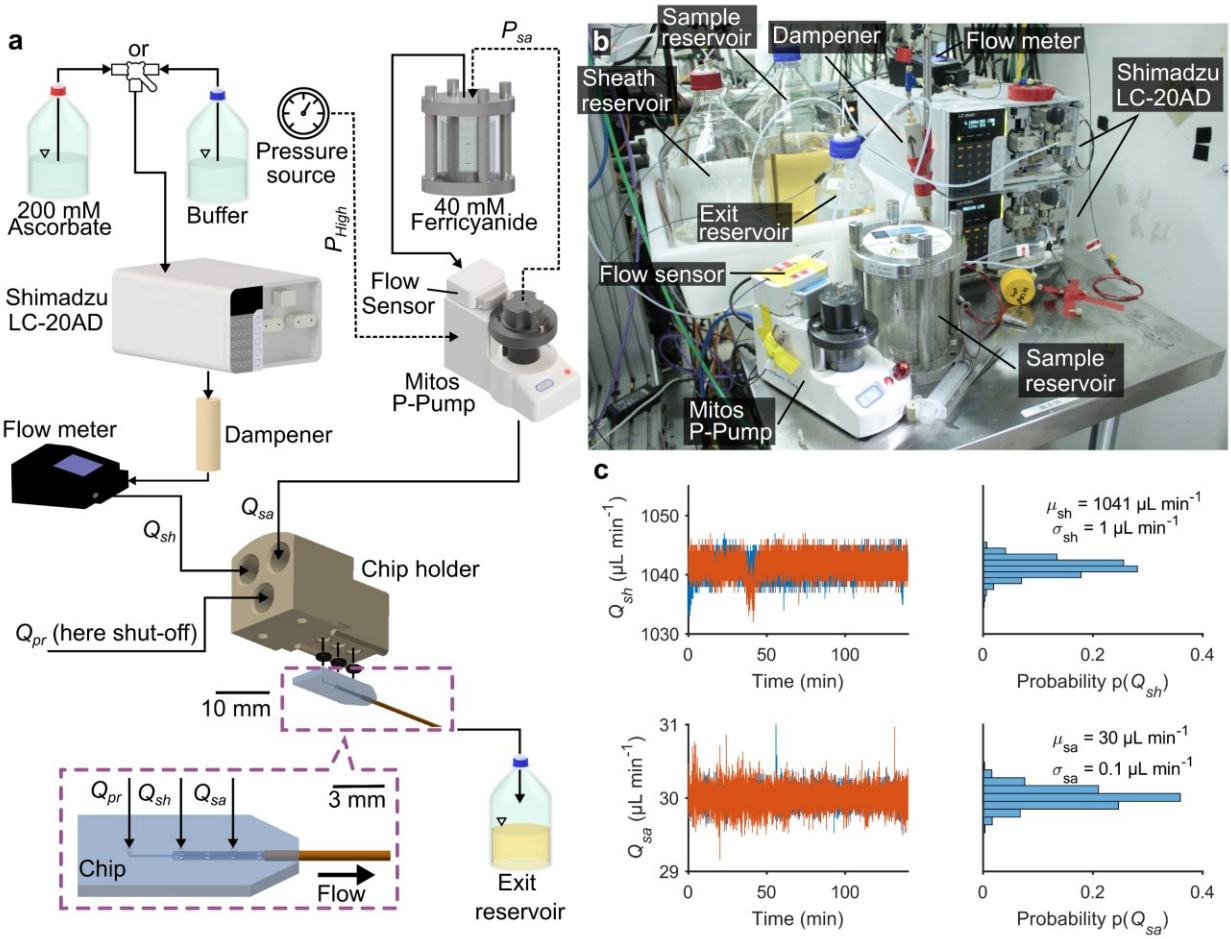

Fig. S7. Schematic, image, and performance demonstration of the experimental fluid flow setup at line 6-2b of the Stanford Synchrotron Radiation Lightsource (SSRL). (a-b) A high-performance liquid chromatography (HPLC) pump (LC-20AD, Shimadzu Corp., Japan) was used to supply the sheath solution (flow rate Q_{sh}) to the chip. The sheath solutions were either 200 mM ascorbic acid H_2Asc or pure buffer. Q_{sh} was maintained near-constant with a custom-made PEEK flow dampener and its value was measured using a flow meter with an accuracy of 0.15% (Flow Meter Standard, CorSolutions, LLC, USA). A pressurized glass vessel (Mitos P-Pump, Dolomite Microfluidic, UK) was used to drive flow of the sample solution (40 mM ferricyanide) at a flow rate of Q_{sa}. Q_{sa} was measured using a flow meter with 5% accuracy (Mitos Sensor Display, Dolomite Microfluidics, UK). Note the third, probe Q_{pr} inlet was shut off for all experiments reported. The region from the capillary to the probe inlet, additionally, was initially filled with water. (c) Raw measurements of Q_{sa} and Q_{sh} versus time (left column) for two independent experiments (blue and orange lines). The mean sample μ_{sa} and sheath μ_{sh} flow rates, as well as the standard deviation of these (σ_{sa} and σ_{sh}, respectively) were calculated from both datasets shown (right column).

S6. Convolutive effect of the X-ray beam

This section demonstrates that measurements of the sample full width at half maximum (FWHM) based on Fe fluorescence data are not ideal due to the large X-ray beam size (Fig. S8).

We are interested in comparing the Fe fluorescent photon flux after X-ray measurements with both predicted and optically measured images of the sample concentration fields. Although the device design was identical in all experiments, assembly imperfections of the system used for the optical experiments resulted in asymmetry in the sample stream (first row of Fig. S9a). The device used during the X-ray experiments, however, did not demonstrate this skewness (Fig. 5c of the main text). Hence, to compare these two images, we chose to track the sample stream expansion along a curvilinear coordinate system (second row of Fig. S9a). This transformation tracks the loci of sample stream concentration maxima (along radial direction) and introduces dimensions parallel and perpendicular to the sample (respectively, s and r). The transformed image is defined as I_{curv}.

For simplicity, we assume the streamwise velocity along this curvilinear coordinate is everywhere equal to the maximum fully-developed velocity field of the symmetric case. We hypothesize that this curvilinear coordinate transformation of the optical case provides a fairer comparison between these two experiments since the quantity of most interest is the Lagrangian history of the radial diffusion of species into/out of the sample stream.

Finally, to recreate the X-ray sampling scheme, we convolved the predicted and optically measured sample concentration fields with a convolution kernel that matched the X-ray beam profile (third and fourth rows of Fig. S9a). This convolution was applied to I_{curv} as follows

$$I_{conv}(s,r) = S_{xy} * I_{curv}$$
$$\int_{s'=-\infty}^{\infty}\int_{r'=-\infty}^{\infty} S_{xy}(s',r') \cdot I_{curv}(s-s', r-r')ds'dr', \tag{8}$$

where S_{xy} is the two-dimensional (2D) beam intensity kernel, and $*$ denotes a convolution. A similar procedure was applied to the predicted, depth-integrated sample concentration fields as

$$[\mathrm{Fe}]_{conv}(x,y) = S_{xy} * [\mathrm{Fe}]_{depth}(x,y). \tag{9}$$

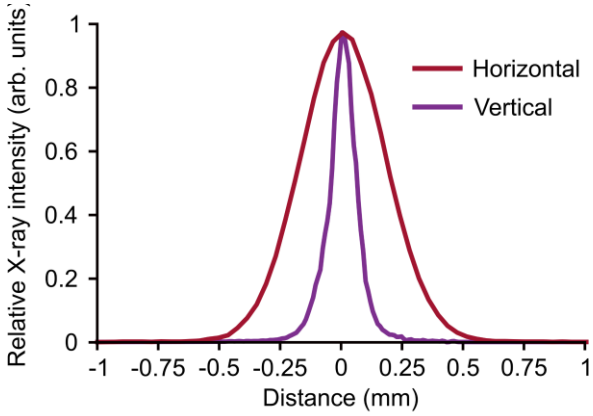

Fig. S8. X-ray beam profile. Shown is intensity versus distance from the center of the beam in the horizontal (streamwise) and vertical (spanwise) directions. The FWHM of the X-ray beam in the

horizontal direction was 418 µm, leading to a footprint of 510 µm along the mixer streamwise direction. The FWHM of the beam in the vertical direction (perpendicular to the flow) was 113 µm.

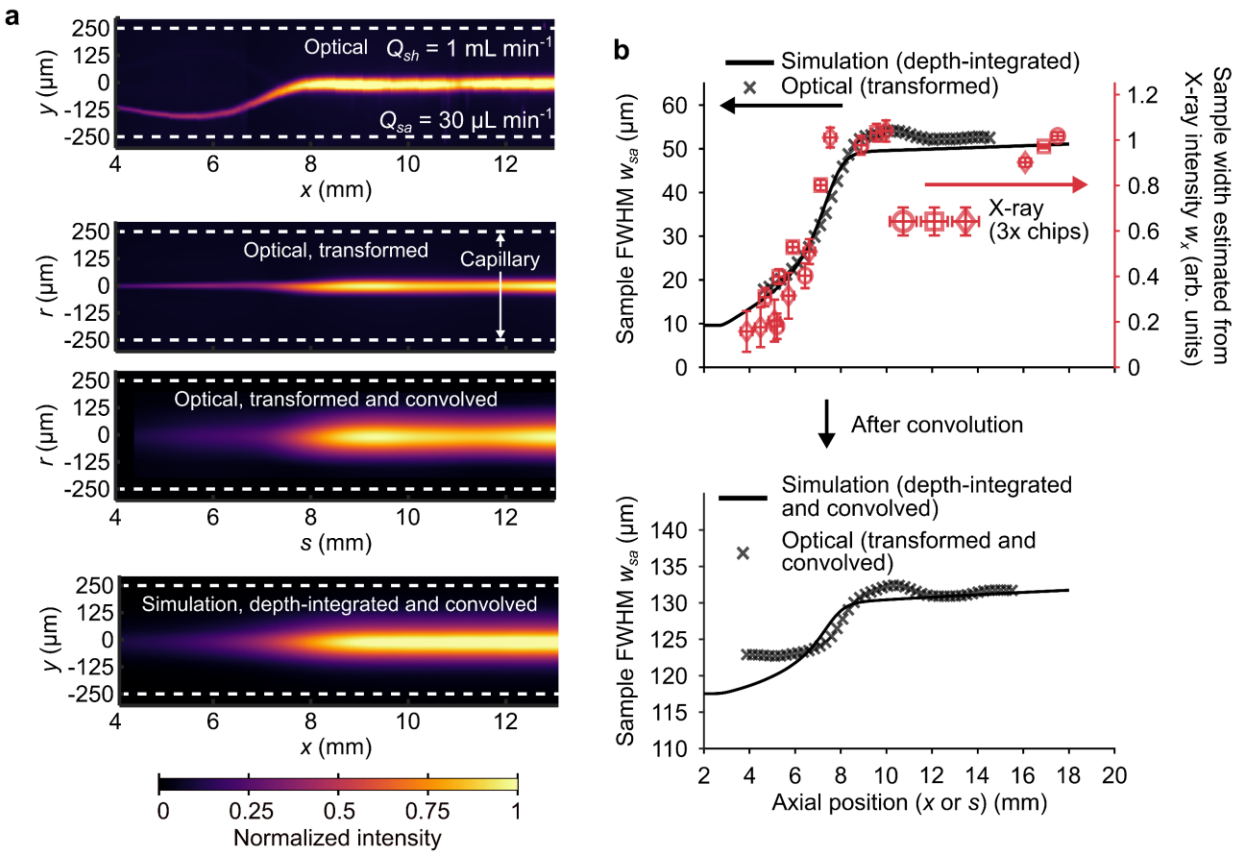

Fig. S9. Streamwise coordinate for optical image and convolutive effect of the X-ray beam. (a) The first image shows an experimental image of fluorescein fluorescence intensity in the downstream capillary region of the mixer. To account for some asymmetry observed in the flow of this setup, the optical image was transformed (second image) based on a curvilinear coordinate system which follows the sample stream light intensity maxima. The transformed optical image was then convolved with the X-ray beam profile (third image) to demonstrate the convolutive effect of the current X-ray detection method. This convolution was also applied to the ferricyanide concentration fields predicted from simulations (fourth image). (b) In the top and bottom plots, the left ordinate (corresponding to the line and circles) is the predicted sample FWHM w_{sa} and the right ordinate (corresponding to the squares) is the sample width associated with the emitted X-ray intensities w_x. Both quantities are plotted versus the sample stream axial position (x for simulations and X-ray measurements and s for optical measurements). As shown by the bottom plot in (b), the convolutive effect of the X-ray beam increases the measured value of w_{sa}. Data in (b) is for the same flow conditions as (a).

S7. UV-Vis Experiments

To probe the mixing characteristics of the microfluidic mixer, we used a reaction with a half-life significantly faster than the expected sample residence time. Ascorbic acid H_2Asc reacts with ferricyanide $Fe(CN)_6^{3-}$ to form ferrocyanide $Fe(CN)_6^{4-}$ and dehydroascorbic acid Asc. When using an excess of ascorbic acid, the reaction follows a pseudo-first order kinetics with a reaction rate depending on the pH value of the solution. The previously published reaction pathway and kinetics (Tonomura *et al.*, 1978) are known for values up to pH = 8 where the reaction is too slow to fulfill the required condition for a sufficiently fast reaction. We performed stopped-flow UV-Vis experiments using a commercially available setup (Biologic, USA) at pH = 10 to determine fast reaction kinetics using concentrations of 0.2, 0.4, and 2.0 mM H_2Asc and 0.04, 0.04, and 0.2 mM $Fe(CN)_6^{3-}$, respectively, in the mixing capillary. The $Fe(CN)_6^{3-}$ solutions were prepared from a 2 mM stock solution while the H_2Asc solutions were prepared from a 40 mM stock solution. Both stock solutions were diluted in a 100 mM carbonate-bicarbonate solution, prepared as described for the X-ray experiments (Appendix D of the main text).

To follow the reaction, we monitored the summed intensity in the region between 400 and 425 nm where only $Fe(CN)_6^{3-}$ absorbs (inset of Fig. S10c). The first-order rate constant k_1 for each of the reactions was determined by an exponential fit of the $Fe(CN)_6^{3-}$ signal versus time (Fig. S10a-c). The second-order rate constant k_2, was then obtained from a linear fit of k_1 versus the ascorbic acid initial concentration $[H_2Asc]_0$, given by

$$k_1\ ([H_2Asc]_0) = k_2[H_2Asc]_0. \qquad (2)$$

The expression above provides a second-order rate constant k_2 = 194.07 mM^{-1} s^{-1} (Fig. S10d).

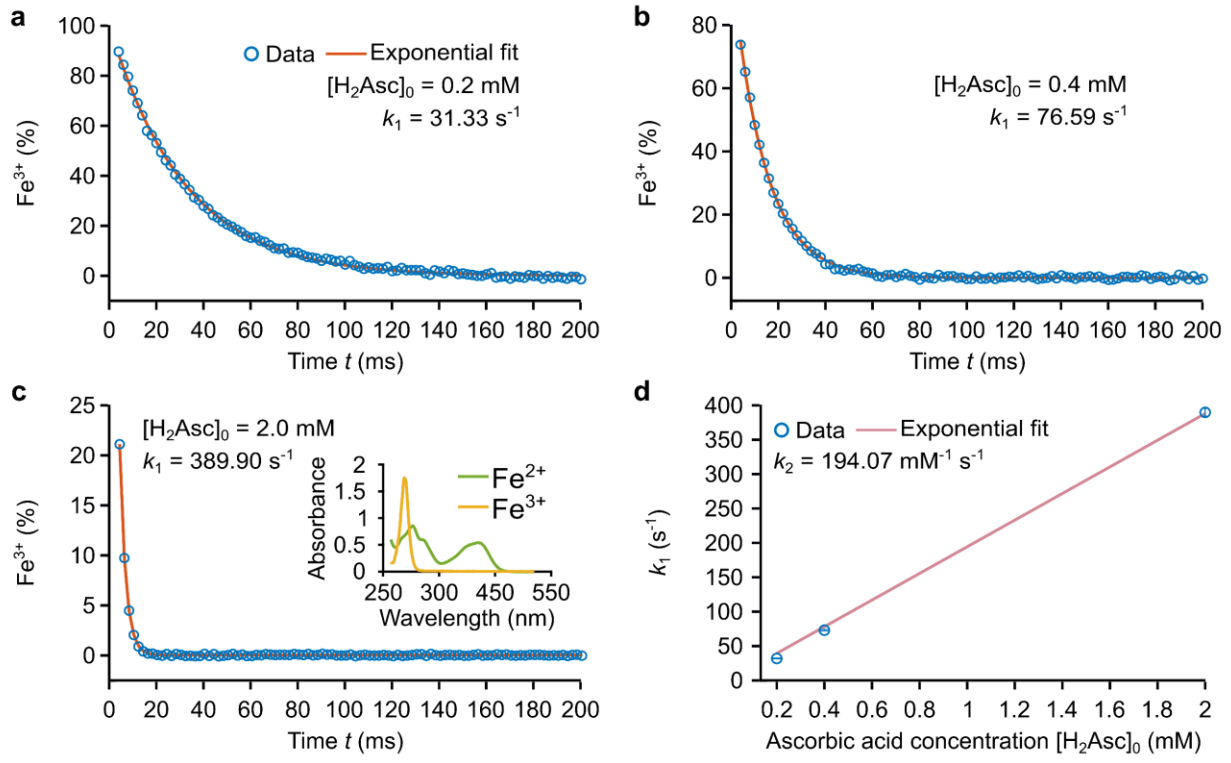

Fig. S10. Results of UV-Vis stopped-flow experiments used to estimate the second order decay rate k_2 of the oxidation of ascorbic acid H_2Asc by ferricyanide $Fe(CN)_6^{3-}$ to dehydroascorbic acid Asc. (a-c) Percentage of unreacted iron Fe^{3+} versus time t for different initial concentrations of ascorbic acid $[H_2Asc]_0$. The inset in (c) shows the reference spectra for Fe^{3+} and the reacted iron Fe^{2+}. (d) Linear fit used to exact the value of k_2. All experiments were performed at pH = 10.

S8. Unmixed sample fraction and residence time at a downstream location

This section reports the predicted depth-averaged, unmixed sample fraction M and sample residence time t as a function of the sample flow rate Q_{sa} or flow rate ratio Q_{sh}/Q_{sa} (Fig. S11). The analysis is performed for sheath flow rates Q_{sh} = 0.5, 1.0, and 1.5 mL min^{-1}.

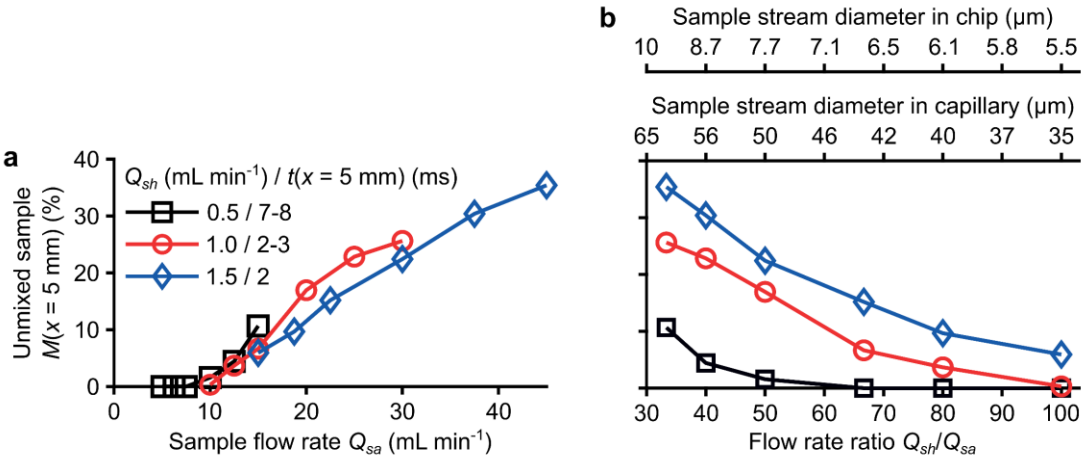

Fig. S11. Predicted depth-averaged, unmixed sample M at a downstream axial position x inside the polyimide capillary (= 5 mm) as a function of flow conditions. (a) $M(x$ = 5 mm) versus the sample flow rate ratio Q_{sa} for various Q_{sh}. The legend also reports a range of sample residence times $t(x$ = 5 mm) for each Q_{sh} (but varied Q_{sa}). (b) $M(x$ = 5 mm) versus Q_{sh}/Q_{sa} (bottom abscissa) and for various Q_{sh} which match those in (a). The two top abscissas show the predicted sample stream diameter in the fused silica chip (0.15 mm < x < 2.87 mm region) and in the polyimide capillary (x > 2.87 mm region). The sample stream diameter, for a fixed geometry, is governed by Q_{sh}/Q_{sa}. The species concentrations and diffusivities match those of Fig. 7 in the main text.

S9. References

COMSOL Inc. (2019). Comsol Multiphysics Reference Manual v. 5.5 Stockholm, Sweden: COMSOL AB.

Culbertson, C., Jacobson, S. & Ramsey, J. (2002). *Talanta*. **56**, 365–373.

Darrall, K. G. & Oldham, G. (1968). *J. Chem. Soc. A Inorganic, Phys. Theor.* **33**, 2584–2586.

Konopka, S. J. & McDuffie, B. (1970). *Anal. Chem.* **42**, 1741–1746.

Muller, P. B., Barnkob, R., Jensen, M. J. H. & Bruus, H. (2012). *Lab Chip*. **12**, 4617–4627.

Phan, H. Van, Coşkun, M. B., Şeşen, M., Pandraud, G., Neild, A. & Alan, T. (2015). *Lab Chip*. **15**, 4206–4216.

Shamim, M. & Baki, S. M. A. (1980). *Aust. J. Chem.* **33**, 1857–1861.
Tonomura, B., Nakatani, H., Ohnishi, M., Yamaguchi-Ito, J. & Hiromi, K. (1978). *Anal. Biochem.* **84**, 370–383.